RESEARCH ARTICLE

Key Points:
- Fault permeability does not affect the timing of the events nor their size
- Injection temperature influences the magnitude of the secondary slip
- Changing the fracture spacing influences the rate of heat energy transfer

Analysis of fluid injection-induced fault reactivation and seismic slip in geothermal reservoirs

Quan Gan[1] and Derek Elsworth[1]

[1]Department of Energy and Mineral Engineering, EMS Energy Institute and G3 Center, Pennsylvania State University, University Park, Pennsylvania, USA

Abstract We explore the issue of fault reactivation induced in enhanced geothermal systems by fluid injection. Specifically, we investigate the role of late stage activation by thermal drawdown. A Thermal-Hydrological-Mechanical simulator incorporating a ubiquitous joint constitutive model is used to systematically simulate the seismic slip of an embedded critically stressed strike-slip fault. We examine the effects of both pore pressure perturbation and thermal shrinkage stress on the magnitude of the resulting events and timing. We analyze the sensitivity of event magnitude and timing to changes in the permeability of the fault and fractured host, fracture spacing, injection temperature, and fault stress obliquity. From this we determine that (1) the fault permeability does not affect the timing of the events nor their size, since fluid transmission and cooling rate are controlled by the permeability of the host formation. (2) When the fractured medium permeability is reduced (from 10^{-13} to 10^{-16} m^2), the timing of the event is proportionately delayed (by a corresponding 3 orders of magnitude). (3) Injection temperature only influences the magnitude but not the timing of the secondary thermal event. The larger the temperature differences between that of the injected fluid and the ambient rock, the larger the magnitude of the secondary slip event. (4) For equivalent permeabilities, changing the fracture spacing (10 m-50 m-100 m) primarily influences the rate of heat energy transfer and thermal drawdown within the reservoir. Smaller spacing between fractures results in more rapid thermal recovery but does not significantly influence the timing of the secondary thermal rupture.

1. Introduction

Massive water injection has the potential to elevate pore pressures within porous and fractured formations and to reactivate faults, either seismically or aseismically [*Cappa*, 2010; *Cappa and Rutqvist*, 2012; *Cappa et al.*, 2009; *Scholz*, 1990; *Segall and Rice*, 1995]. Extensive studies have explored the response of injection-induced activity in enhanced geothermal systems (EGS): some evidence shows that the stress perturbation and the elevation of fluid pressures may induce distributed seismic events on fractures [*Zoback and Harjes*, 1997]. However, reactivation, especially on large faults, may result in large seismic events [*Garagash and Germanovich*, 2012], depending on the weakening characteristics of the feature [*Miller et al.*, 2004; *Segall and Rice*, 1995].

Possible mechanisms of fault reactivation are not limited to hydromechanical effects. In geothermal systems where the reservoir is chilled with the forced-circulation of cold fluid, the induced thermal shrinkage stress will also control changes in effective stress and may cause fault activation and induced seismicity [*Rutqvist and Oldenburg*, 2007; *Rutqvist et al.*, 2008]. Stresses reduce as convective transport drains heat from the rock matrix and it thermally shrinks and decompresses along the unloading curve according to the equivalent elastic properties of the fractured medium [*Bažant et al.*, 1979; *Boley*, 1960; *Sandwell*, 1986].

Since energy release is proportional to fracture aperture to the third power—representing the effective volume destressed by the slip—large faults are of significant concern when understanding reactivation. Large faults (finite thickness) typically have a specific architecture including heterogeneous properties of a fault core zone and damage zone [*Caine et al.*, 1996] that exert a strong influence on fluid transport behavior. This includes a low-permeability fault core that is a flow barrier across the fault and flanked by higher (than the host) permeability zones [*Faulkner et al.*, 2003; *Kim et al.*, 2004; *Vermilye and Scholz*, 1998].
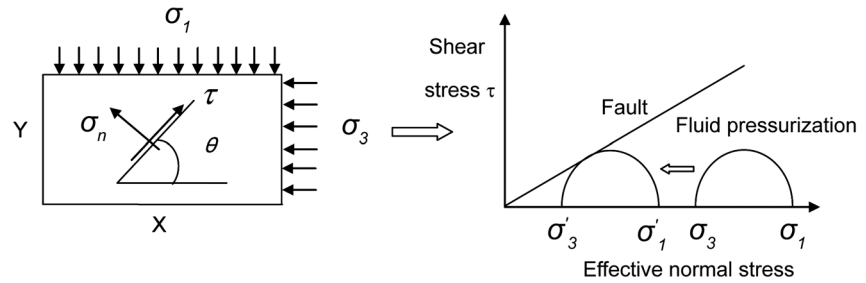
Figure 1. (left and right) Fault plane stress analysis and slip failure mechanism by fluid pressurization.

The fault core is typically gouge filled with low permeability (in the range 1×10^{-17} to $1 \times 10^{-21} \, m^2$). Significantly, the impermeable fault acts as a barrier to prevent water from penetrating through the fault although fault-parallel transmission is possible. Fault reactivation is a complex process involving the interaction of total stresses and fluid pressures and transformations in stiffness and permeability. In this work we focus on the additional impact of delayed thermal stresses on the timing and magnitude of any induced instability.

We use a coupled Thermal-Hydrological-Mechanical (THM) model [*Taron and Elsworth*, 2009, 2010] to explore the different factors governing fault reactivation of a critically stressed strike-slip fault. The critical controlling parameters that are examined include fault permeability, fractured medium permeability, fracture spacing, and stress obliquity relative to the fault. Finally, we control the temperature of the injected water as a method to scale the impact of thermal effects.

2. Model Setup

In order to investigate the influence of fluid pressures and thermal stresses on the reactivation of critically stressed faults, we analyze anticipated stress changes using a simple model for a fault acted upon by far-field stresses. This defines the stress drop, which in turn may be used to define the seismic energy release and related event magnitude. We then follow the development of stresses around faults oriented with different stress obliquities using a suitable simulator that couples the effects of fluid transport and changes in total stresses. This method is used to evaluate the timing and magnitude of the resulting slip events.

2.1. Analytical Stress Analysis

Normally, fault instability is governed by contemporary principal stress orientations relative to the preexisting fault planes [*Streit and Hillis*, 2004]. Based on effective stress theory and the Coulomb failure criterion, the basic equation for slip on a plane is defined as

$$\tau = C + \mu_s(\sigma_n - p) = C + \mu_s \sigma_{neff} \tag{1}$$

where C is the cohesion, p is the fluid pressure, μ_s is the coefficient of friction, σ_n is the normal stress, and τ is the shear stress [*Scholz*, 1990].

To allow the analysis of failure due to an applied oblique stress on the failure of a preexisting fault [*Jaeger*, 1979], the effective normal stress σ_{neff} and shear stress τ along the fault may be defined as (see Figure 1)

$$\sigma_{neff} = \frac{\sigma_x + \sigma_y}{2} + \frac{\sigma_x - \sigma_y}{2} \cos 2\left(\frac{\pi}{2} - \theta\right) - \tau_{xy} \sin 2\left(\frac{\pi}{2} - \theta\right) - p \tag{2}$$

$$\tau = \frac{\sigma_x - \sigma_y}{2} \sin 2\left(\frac{\pi}{2} - \theta\right) - \tau_{xy} \cos 2\left(\frac{\pi}{2} - \theta\right). \tag{3}$$

To allow stability to be determined when combined with the strength criterion,

$$\tau_s = \sigma_{neff} \cdot \mu_s. \tag{4}$$

This enables strength of a rock mass incorporating a single plane of weakness to be straightforwardly evaluated [*Jaeger*, 1979]. Where we assume that failure may occur on the most critically oriented plane
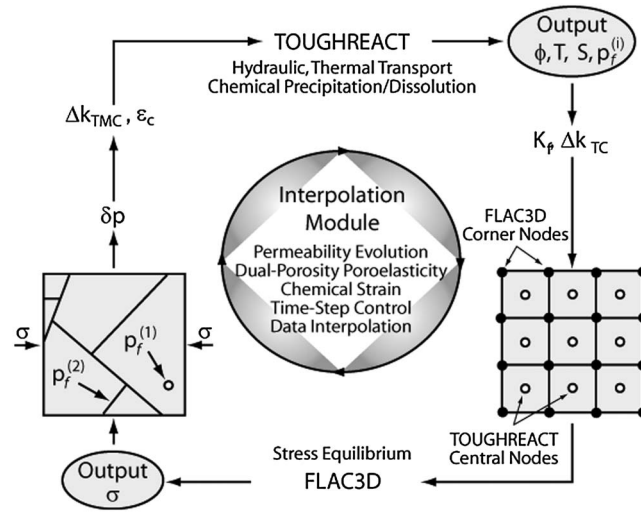
Figure 2. FLAC-TOUGH model simulation flow chart [*Taron and Elsworth*, 2009].

(Figure 1, right), then the ratio of maximum and minimum principal effective stresses is given by [*Rutqvist and Oldenburg*, 2007]

$$\frac{\sigma_1'}{\sigma_3'} = \frac{\sigma_1 - \alpha p}{\sigma_3 - \alpha p} \leq q$$

$$= \left[\left(\mu_s^2 + 1 \right)^{1/2} + \mu_s \right]^2 \qquad (5)$$

where q represents the effective stress limiting difference ratio, where we adopt Biot effective stress theory [*Biot*, 1941] to calculate the horizontal effective maximum in situ and minimum in situ stress. When the left-hand side ratio exceeds q, then the fault begins to slip. In our study, the Biot coefficient is set as 0.8; the internal fault friction angle is equal to 28° and

therefore $\mu_s = 0.53$ [*Biot*, 1941; *Byerlee*, 1978], so the value of q is 2.76; and the friction angle of the intact host rock is 30° and then the corresponding value q is 3. Correspondingly, for the stress regime of $\sigma_1 = 45.5$ MPa, $\sigma_3 = 28.6$ MPa, and $p = 18.1$ MPa the stress obliquity is $J = \sigma_1'/\sigma_3' = 2.2 < q = 2.76$.

Therefore, the fault is set as initially stable, while critically stressed. An approach to describe the fault slip potential could use the parameter Δ

$$\Delta = \Delta\sigma_1' - 2.76\Delta\sigma_3' \qquad (6)$$

where $\Delta\sigma_1'$ represents the change in maximum principal effective stress and $\Delta\sigma_3'$ is the change in minimum principal effective stress.

In this work, the failure potential is estimated using a friction angle of 28° and zero cohesion; therefore, failure occurs when the effective stress ratio $J = \sigma_1'/\sigma_3'$ is greater than 2.76.

2.2. TOUGH-FLAC Simulator Introduction

We use a coupled Thermal–Hydrologic–Mechanical–Chemical model [*Taron and Elsworth*, 2009] capable of representing the mechanical response of the fractured porous subsurface due to fluid injection and recovery. This model satisfies the requirement of representing the coupled elastic-plastic behavior of the fault. The simulator couples analysis of mass and energy transport in porous fractured media (TOUGH) and combines this with mechanical deformation (FLAC3D) as noted in Figure 2 [*Xu et al.*, 2003, 2004, 2001]. The same meshes are used for each of these codes, although TOUGH has block-centered nodes and FLAC3D nodes at the block corners (see Figure 2). Thus, interpolation is required between pressures defined in the transport model to be applied as effective stresses in the mechanical code (TOUGHREACT). Evolving effective stresses are used, together with an appropriate constitutive model to define the evolution of fracture apertures in the medium and to thereby determine the change in permeability.

2.3. Fault Modeling Approach

Generally, there are three approaches to model fault characteristics [*Cappa*, 2010; *Rutqvist et al.*, 2002]: the fault could be characterized as a mechanical interface with zero thickness, by representation with solid elements and double interfaces or by combination of solid elements and ubiquitous joints as weak plane (see Figure 3). Fault modeling as an interface could be an appropriate approach if the thickness of the fault is negligible compared to the scale of the entire reservoir. To successfully couple fault slip with fluid pressurization in an interface model, it is necessary to add hydraulic elements along the interface, because the hydraulic elements must update the effective normal stress and shear strength by interpolating accurate
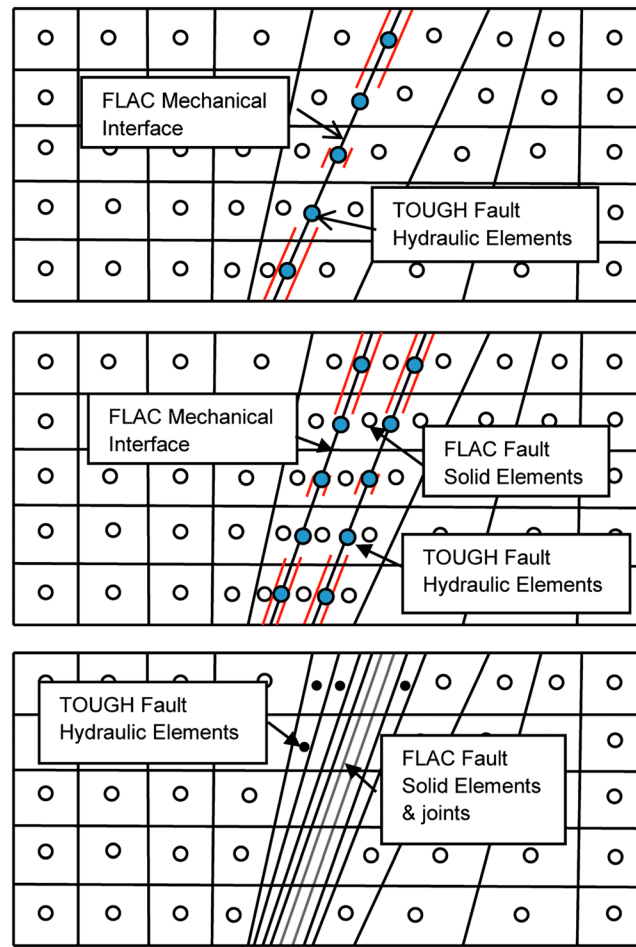
Figure 3. Available approaches for fault modeling in TOUGHREACT.

fault pressure. However, this approach is difficult in building the fault gridding in TOUGH; and it cannot model the heterogeneous character of the fault. The continuum approach with a ubiquitous joint constitutive model in FLAC3D is easier in building meshes for TOUGH; furthermore, this approach can represent the anisotropic plasticity of the fault by accounting for the presence of a weak plane. Therefore, we adopt this third approach to model the fault.

2.4. Moment Magnitude Scaling

The seismic energy released by shear slip on a preexisting fault plane is quantified by the event moment M_0. The moment magnitude scale M_S is used to measure the strength of the seismic event. The M_S-M_0 relationship is defined [*Kanamori and Abe*, 1979; *Purcaru and Berckhemer*, 1982] as

$$\log M_0 = 1.5 M_s + 16.1 \qquad (7)$$

where M_0 is seismic moment and M_s is moment magnitude.

The moment M_0 is also defined by the relation [*Aki*, 1967],

$$M_0 = \mu L W D_c \qquad (8)$$

where L = fault length, W = fault rupture width, μ = rigidity, and D_c = slip distance.

The fault seismic moment is a function of slip distance and fault rigidity when the fault rupture area is constant. Since the different patches on the fault undergo different slip distances due to the decaying propagation of the rupture front along the fault, we define the moment by the following equation:

$$M_0 = \int_0^L \mu L W \mathrm{d}D_c. \qquad (9)$$

In order to obtain moment magnitudes that are appropriate to the 3-D representation of the fault (fault area of 442 m × 442 m), we use the results from the 2-D plane strain model and extrapolate these over the fault area. This switch between the 2-D slip model and the 3-D fault ignores the clamped boundaries (zero displacement) at the top and base of the fault and would slightly overestimate the moment magnitude —relative to the real case where the edges of the fault are clamped.

2.5. Model Configuration

The model is used to represent conditions prototypical to an enhanced geothermal system (EGS). The reservoir geometry is a pseudo 3-D doublet (1500 m × 600 m × 15 m) (see Figure 4). The initial temperature distribution is homogeneous with an initial rock temperature of 250°C. The minimum in situ stresses are imposed at 28.8 MPa in the W-E direction, and maximum in situ stresses are subjected to a constant 45 MPa in the N-S direction. A strike-slip fault is located in the center of reservoir with the injection well and withdrawal well distributed to the east and west of the fault, respectively. In this configuration the fault acts as a barrier
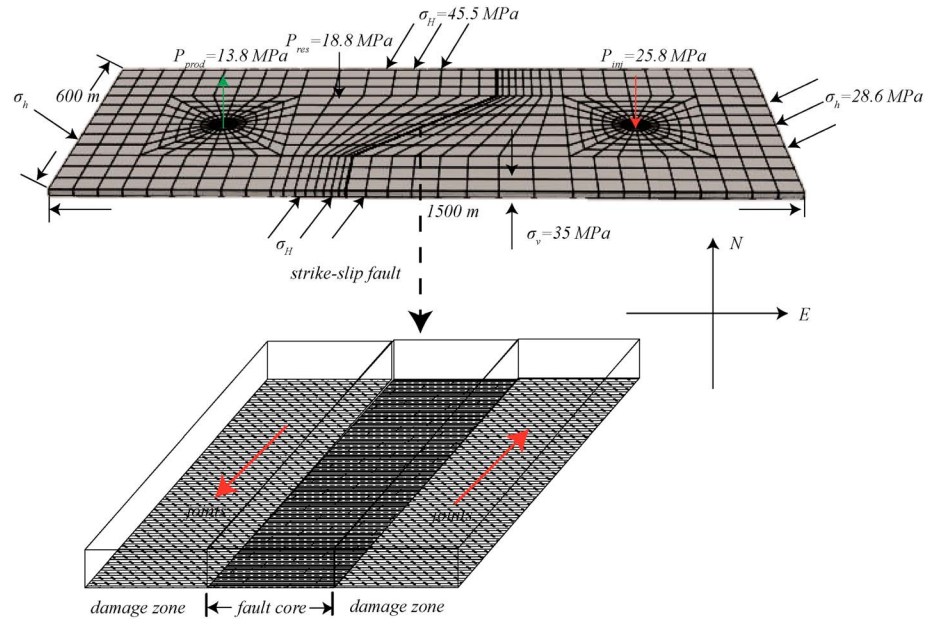
Figure 4. (top) Model geometry and applied stress boundary condition, initial condition, and (bottom) strike-slip fault geometry in model.

for the propagation of the fluid front from the injection to the recovery well. The model boundaries are set as no-flow boundaries with applied constant stresses.

The strike-slip fault comprises a low-permeable core (thickness 0.8 m) and flanked by higher permeability damage zones (thickness 1.2 m). The ubiquitous joint model represents the elastic-plastic behavior of the fault. The joints and host rock have the same initial internal frictional angle of 28° (see Table 1). We adopt a linear strain-softening relationship that implies that the friction angle decreases with an increase in the plastic strain.

3. Validation Result

We use the geometry of Figure 4a to validate the model. The simulation results in induced fault seismic slip due to over pressurization by the fluid (2 MPa). The parameter $J = \sigma_1'/\sigma_3'$ is utilized to describe the distribution of shear failure potential (see Figure 5) around the pressurized fault. When the fault friction angle is equal to 28°, the fault and areas ahead of the tip show a high potential for slip, as illustrated by $J > 2.76$ (Figure 5a). This strength is applied on the fault, but the strength in the surrounding matrix corresponds to a friction angle equal to 30° with $J = 3$ that remains unfailed in the matrix. Where strength of the fault is raised to 35° and the analysis completed, the fault is now stable (Figure 5b with $J > 3.7$ required for failure) despite the same 2 MPa over pressurization.

During failure, the control point in the center of the fault has the largest relative seismic slip distance of 0.35 m (see Figure 6b). The corresponding seismic moment magnitude is 3.1. When the rupture front migrates away from the center of the fault to the fault tips, the slip distance of each patch decreases. When

Table 1. Material Properties Input in Model [*Rutqvist et al.*, 2013]

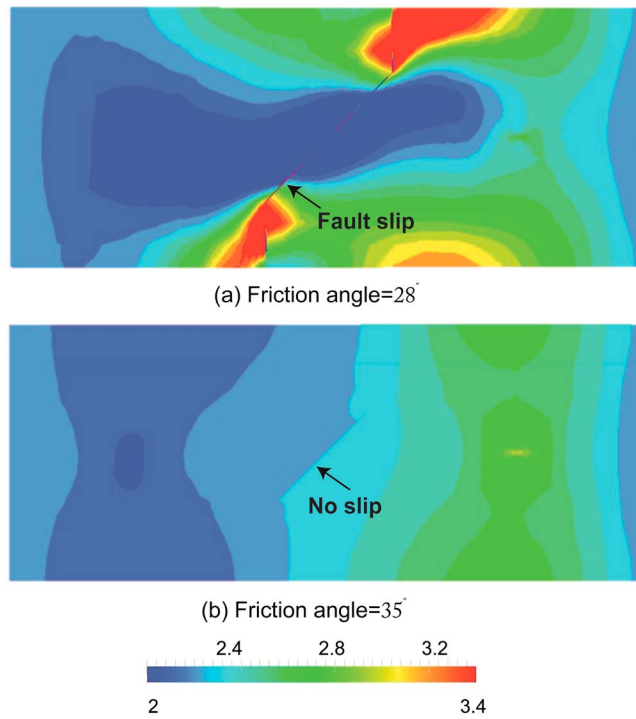| Parameters	Intact Rock	Damage Zone	Core Zone
Young's modulus (GPa)	8	1.5	1.5
Shear modulus (GPa)	5.5	1	1
Permeability (m²)	1×10^{-13} to 1×10^{-16}	1×10^{-14} to 1×10^{-17}	1×10^{-19}
Poisson's ratio	0.2	0.2	0.2
Friction angle	30	28	28
Fracture porosity	0.8	0.8	0.8

Figure 5. (a and b) Spatial distribution of the fault failure potential, *J*, under isothermal injection.

the slip occurs, the corresponding Coulomb Stress ratio is equal to the tangent of the friction angle tan28° (see Figure 6c).

4. Parametric Analysis

To understand the principal factors that influence event magnitude and timing during fault reactivation, we examine the influence of fault and host permeability, fracture spacing of the host, injection temperature, and
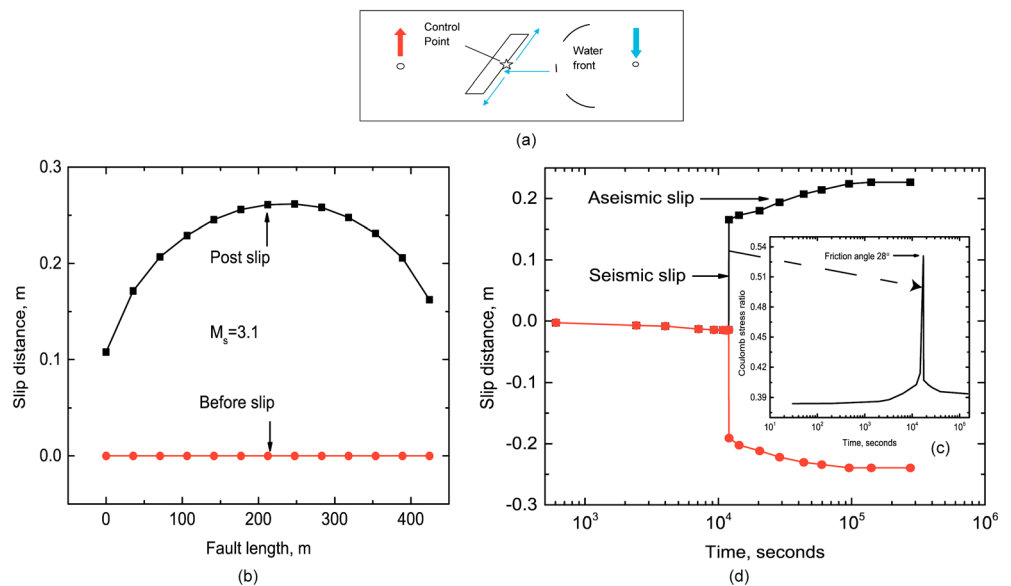

Figure 6. Response at control points (a) located at midlength on the fault and (b) resulting fault slip distance distribution for cases both before and after slip. (c) Evolution of Coulomb stress ratio at midlength along the fault. (d) Slip distance along the fault under isothermal injection.
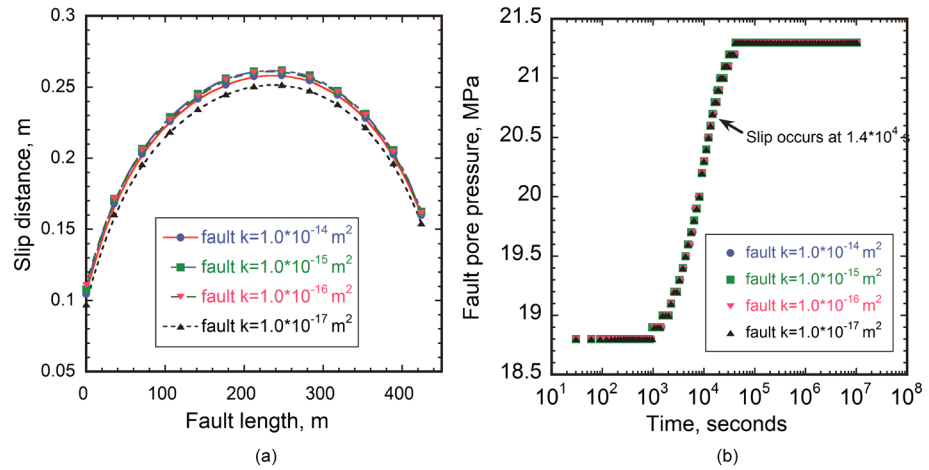
Figure 7. (a) Fault slip distance distribution comparison under different fault permeability and (b) fault pore pressure evolution comparison under different fault permeability.

stress obliquity. These factors are evaluated during the full loading cycle including the influences of fluid pressure and thermal stresses, respectively, at early and late times during reservoir production.

4.1. Fault Permeability

The hydraulic characteristics of the fault are represented by a low-permeability core [*Caine et al.*, 1996] flanked by damage zones with elevated permeability and embedded within the host medium of defined intermediate permeability. The permeability of the fault damage zone is varied from $10^{-14}\,m^2$ to $10^{-17}\,m^2$, with the fracture permeability of the host is $10^{-14}\,m^2$.

Figure 7a shows the evolution of the fault slip distance at the control point for different fault damage zone permeability values. The overpressure required to induce slip is sensibly constant in all cases (total stresses do not change significantly), and since pressure buildup in the fault is controlled principally by supply of fluid through the moderate permeability ($10^{-17}\,m^2$) fractured host, then the timing of fault slip is the same for different fault permeabilities. In all cases, the slip occurs ~3.9 h (1.4×10^4 s) after the initiation of pumping (see Figure 7b).
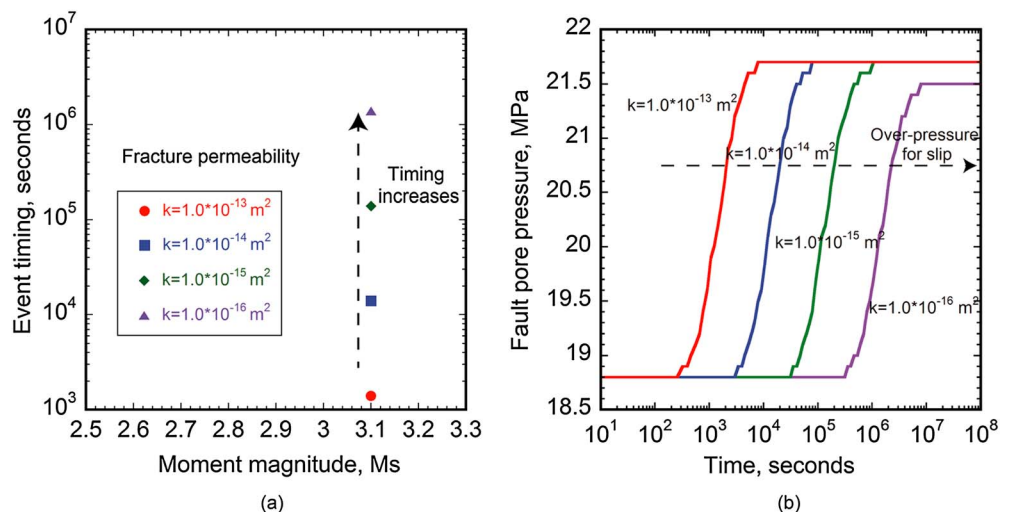

Figure 8. Fault seismic slip (a) event timing versus magnitude under different fracture permeabilities and (b) fault pore pressure evolution under different fracture permeabilities.
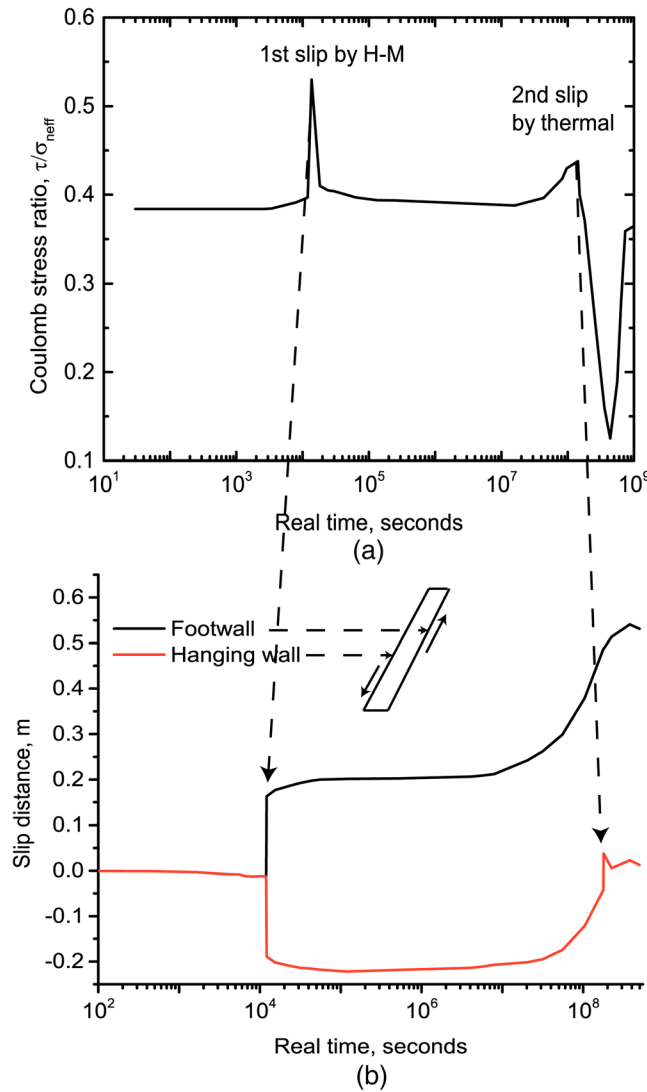
Figure 9. Two fault seismic slips occurred within 20 years induced by H-M effect and by cooling stress effect. (a) The evolution of fault Coulomb stress ratio. (b) Slip distance evolution of both footwall (green line) and hanging wall (blue line).

4.2. Fractured Medium Permeability

As noted previously, the permeability of the fractured host controls pressure buildup in the system by limiting the supply of fluid to the embedded fault. Thus, where permeability of the host is either initially elevated, or where it is similarly increased by artificial stimulation, then this will influence the rate of fluid supply to the fault. This further modulates the timing of slip. For a fractured medium the growth in the fracture aperture may be defined by an empirical function of nonlinear fracture stiffness α and applied effective stress σ [*Rutqvist et al.*, 2002] as

$$b_m = b_{mr} + (b_{mo} - b_{mr}) \exp(-\alpha\sigma) \quad (10)$$

where b_m denotes the hydraulic aperture due to mechanical stress effect alone, b_{mo} is the aperture without mechanical stress effect, and b_{mr} is the residual aperture solely under the mechanical stress. Assuming that the mechanical aperture is approximately equivalent to the hydraulic aperture ($b \sim b_m$) in an orthogonally fractured medium, then the permeability may be defined as

$$k = \frac{b^3}{12s} + \frac{b^3}{12s} = \frac{b^3}{6s} \quad (11)$$

where s is the fracture spacing and b is fracture aperture. The fracture permeability is dynamic due to controls on the evolution aperture exerted by mechanical stress effects.

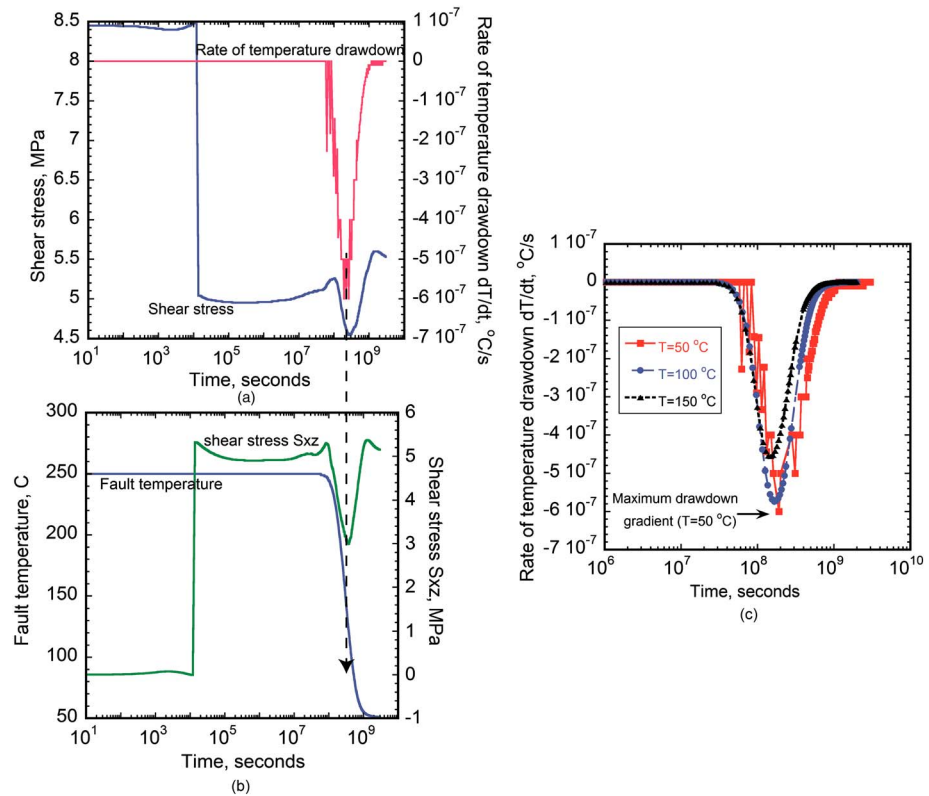We examine the influence of feasible permeabilities of fractured host in the range $10^{-13} - 10^{-16}\,\text{m}^2$ on the magnitude and timing of fault slip where the permeability of the fault damage zone is maintained constant at $10^{-15}\,\text{m}^2$. In all cases, the fracture spacing is retained constant at 10 m.

Figure 8 shows that high fracture permeabilities concomitantly decrease the time taken for the pressure front to arrive at the fault and to build to the required fault reactivation pressure of 20.7 MPa. For this pressure-controlled system the delay in fault reactivation increases by almost an order of magnitude for each 1 order decrease in fracture permeability: the fault slips at 0.38 h (1.4×10^3 s) when the host permeability is $10^{-13}\,\text{m}^2$ and 3 orders of magnitude later 16.2 days (1.4×10^6 s) when the host permeability is decreased to $10^{-16}\,\text{m}^2$. However, although slip occurs earlier as the permeability is increased, the relative slip distance of the fault remains the same—resulting in no change in moment magnitude with this change in host permeability (Figure 8a).

4.3. Injection Temperature

With the prior influence of isothermal injection examined for differences in permeability of both the fault and the host, we now examine the influence of thermal drawdown (nonisothermal injection) on fault reactivation.

Figure 10. (a) Fault shear stress (blue) and fault temperature drawdown gradient (red) evolution, (b) the evolution of fault temperature + (blue), and (c) comparison of fault thermal drawdown gradient under different water injection temperatures ($T = 5°C, 100°C$, and $150°C$).

Specifically, we are interested in the potential for late-time reactivation due to the stresses induced by thermal drawdown.

Figure 9 confirms that indeed late time seismic events may occur within the 30 year injection history when fluid is injected at 50°C into a host of 250°C, where the fracture host permeability is kept as $10^{-14} m^2$ and the fault permeability is $10^{-17} m^2$. The first seismic slip event occurs due to hydromechanical effects at $1.4 \times 10^4 s$ (3.9 h), and the second slip occurs at 1.4×10^8 s (4.4 years) when the thermal front arrives at the fault and causes significant temperature drawdown. The magnitude of the second slip event that is induced by the thermal shrinkage stress is weaker than the first event induced by hydromechanical effects. The first event has a relative slip distance of 36 cm and a magnitude of 3.1 with the second event displacing only 6 cm with a magnitude of 2.6.

When the hot reservoir rock is cooled, the thermal stress induced by shrinkage results in unloading by decreasing the maximum in situ stress, and in turn, the fault shear strength decreases. The associated decrease in shear strength in the cooling regime facilitates fault reactivation. Figure 10a shows that the seismic slip induced by the thermal stress occurs when the rate of temperature drawdown gradient reached to the maximum point. Figure 10c indicates that the maximum drawdown gradient at an injection temperature $T = 50°C$ is a critical transition point for inducing late-stage seismicity. In this particular instance, the maximum absolute value of the thermal drawdown gradient is equal to $6 \times 10^{-7} °C/s$. Figure 10b shows that the fault temperature begins to be drawn down after 8.0×10^7 s (2.5 years), and this continues until the reservoir is depleted after 1.6×10^9 s (50.7 years).

The effect of the thermal shrinkage stress is most pronounced at the thermal boundary between the hot and cooling regions where stress gradients are largest. Displacements in the direction of the minimum principal stress indicate a net displacement into the cooled region as that region thermally compacts
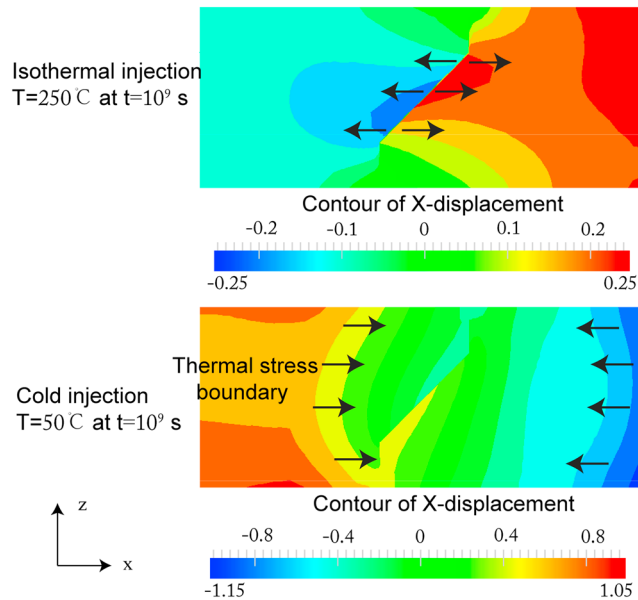
Figure 11. Field x displacement distribution for isothermal injection and cold injection.

(see Figure 11). Slip occurs when the advancing cooling front reaches the fault and the rate of stress change, both in space and in time, is particularly high (Figure 10). Therefore, we primarily investigate the influence of injected fluid temperature in the range $50°C - 250°C$ on the magnitude and timing of fault slip and thermal energy recovery efficiency. Figure 12 shows that the timing and magnitude of the first seismic slip event is not affected by the injection temperature, because the hydraulic front diffuses faster than the thermal front, so the first seismic slip event induced by hydraulic-mechanical effects are not affected by the temperature variation of the injected fluid. However, it is observed that only the colder injection ($T = 50°C$) causes sufficient fault shear strength reduction and in turn slips at $t = 1.4 \times 10^8$ s (4.4 years), and as expected, the injected fluid with hotter temperature does not generate the later time seismic slip event. The greater temperature difference between the injected fluid and the ambient rock results in larger thermal stress, which reduces the fault shear strength to a larger extent. Thus, only the colder injection leads to a larger seismic fault reactivation.

4.4. Fracture Spacing

The injected fluid flows only in the fractures and the fracture spacing directly controls thermal conduction from the matrix to the fluid in the fractures. Here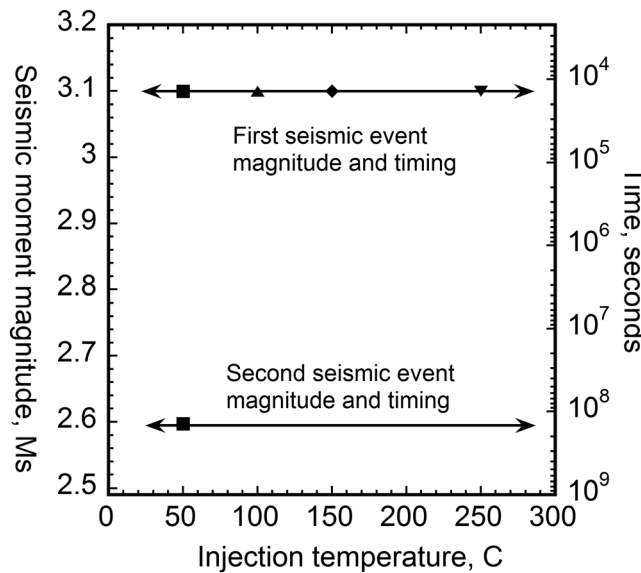 we investigate the influence of fracture spacing (10 m 50 m and 100 m) in both fault reactivation and heat energy recovery efficiency, while the fracture permeability is retained constant at 10^{-14} m^2.

To determine the impact of fracture spacing on thermal recovery and fault slip, we compare the results for isothermal injection ($T = 250°C$) to those for cold injection ($T = 50°C$) and with different fracture spacing. Figure 14 illustrates that the variation in fracture spacing has no impact on the timing and magnitude of fault reactivation; in all cases, the fault slips after ~1.4×10^4s (3.89 h) under isothermal injection $T = 250°C$. Similarly, they are unchanged for cold injection; the timing of the second (thermally activated) slip

Figure 12. Fault seismic event magnitude and timing result comparison under different injection temperature 50°C, 100°C, 150°C, and 250°C. The arrows in the left direction show the results of event magnitude, and the arrows in the right direction show the results of event timing.
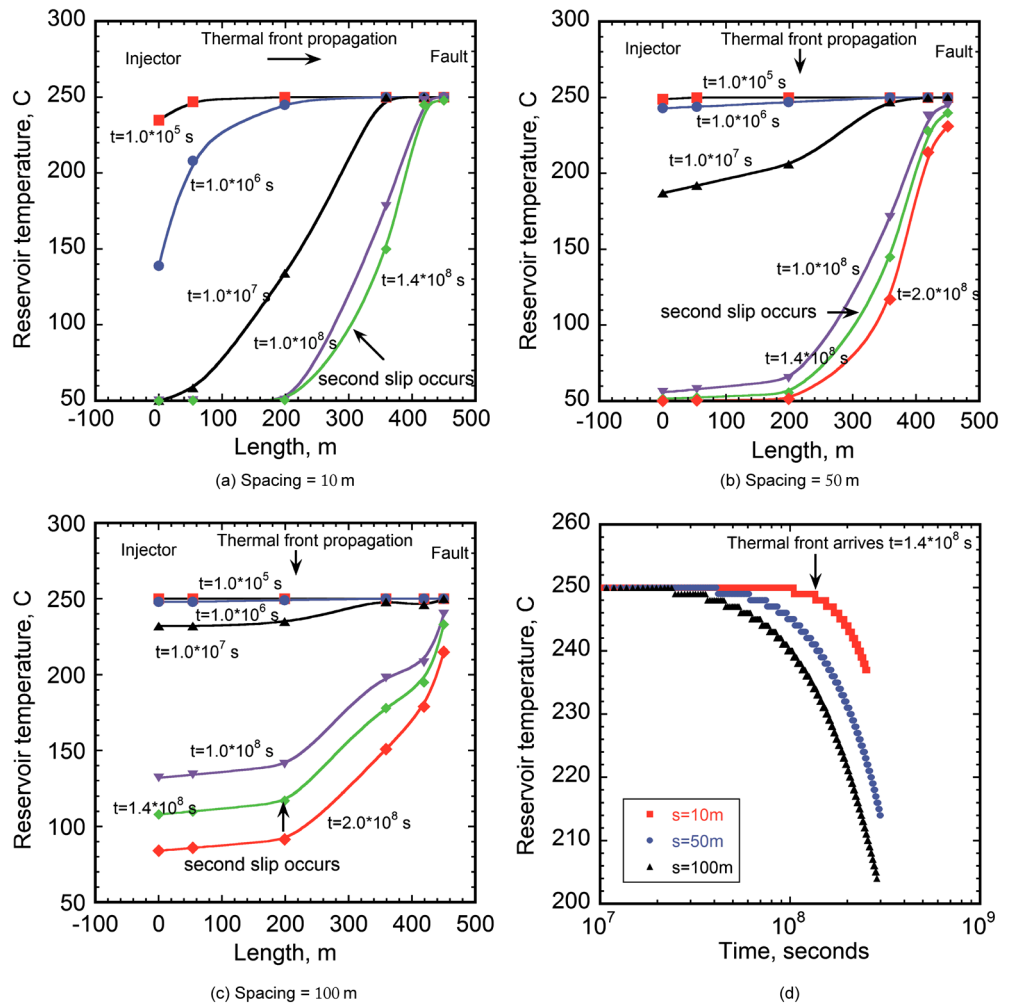
Figure 13. (a) Reservoir temperature evolution under fracture spacing = 10 m, (b) reservoir temperature evolution under fracture spacing = 50 m, (c) reservoir temperature under fracture spacing = 100 m, and (d) fault temperature evolution under 10 m-50 m-100 m fracture spacing.

for all the fracture spacing cases (10 m-50 m-100 m) remains unchanged at ~1.4 × 10^8 s (4.43 years), and the corresponding seismic moment magnitude is 2.6. Figure 13a shows that the thermal front propagates uniformly at small fracture spacing (10 m) in the reservoir, and the second (thermally activated) slip event is triggered as soon as the thermal front arrives at the fault at ~1.4 × 10^8 s (4.43 years). Conversely, when the fracture spacing is increased to 100 m, the reservoir temperature decreases uniformly across the reservoir without the presence of a distinct thermal front. The spatial thermal gradient around the fault is the principal factor to determine whether the second slip event actually occurs (Figures 13b and 13c). It indicates that the spatial thermal gradient is maximum at ~1.4 × 10^8 s (4.43 years) and is similar for fracture spacing between 50 m and 100 m.

Further investigation of the temperature profiles reveals that the denser fracture spacing increases the residence time of the cold fluid circulating within the hot reservoir, and the smaller fracture spacing allows more rapid recovery of heat from the matrix blocks (Figure 14). Figures 15a show the evolution of fluid temperature within the reservoir for different fracture spacing ($T = 50°C$). As fracture spacing increases, the chilled region adjacent to the injector is reduced in size (see Figure 15b). Thus, the more closely spaced fractures result in a faster recovery of heat from the reservoir.

4.5. Stress Obliquity

Fault orientation plays an important role in modulating the stress state on the fault plane and in controlling the fluid overpressurization required for fault reactivation. We compare different fault orientation scenarios
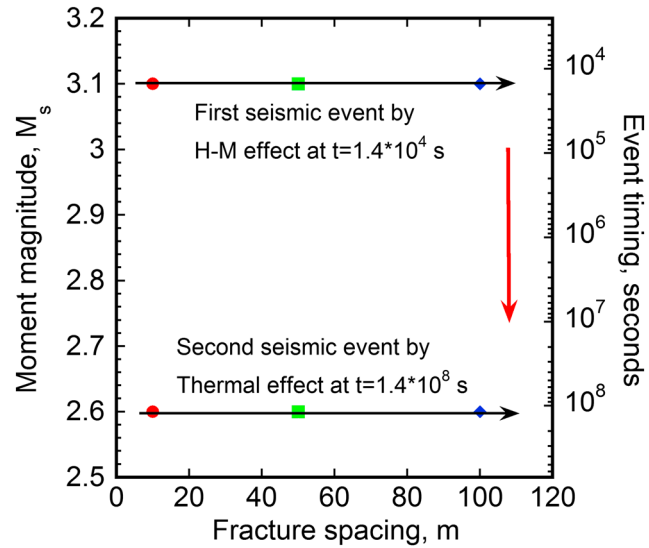
Figure 14. Fault seismic slip event magnitude and timing comparison under different fracture spacing (injection temperature $T = 50°C$).

while maintaining the distance between the fault center and injection well as constant. During this, the fault plane angle is varied from 30° to 75° (see Figure 16a).

The fault is stable when the fault is inclined at only 30° but fails with the largest slip distance (6 cm) and moment magnitude (2.5) occurring after 1.4×10^4s (3.9 h) when inclined at 60° to the minimum principal stress (Figure 16b). This is for H-M effects only.

5. Conclusions

We explore the potential for reactivation of a major strike-slip fault in an enhanced geothermal systems (EGS) reservoir. We systematically investigate the mechanisms causing fault reactivation and seismic slip
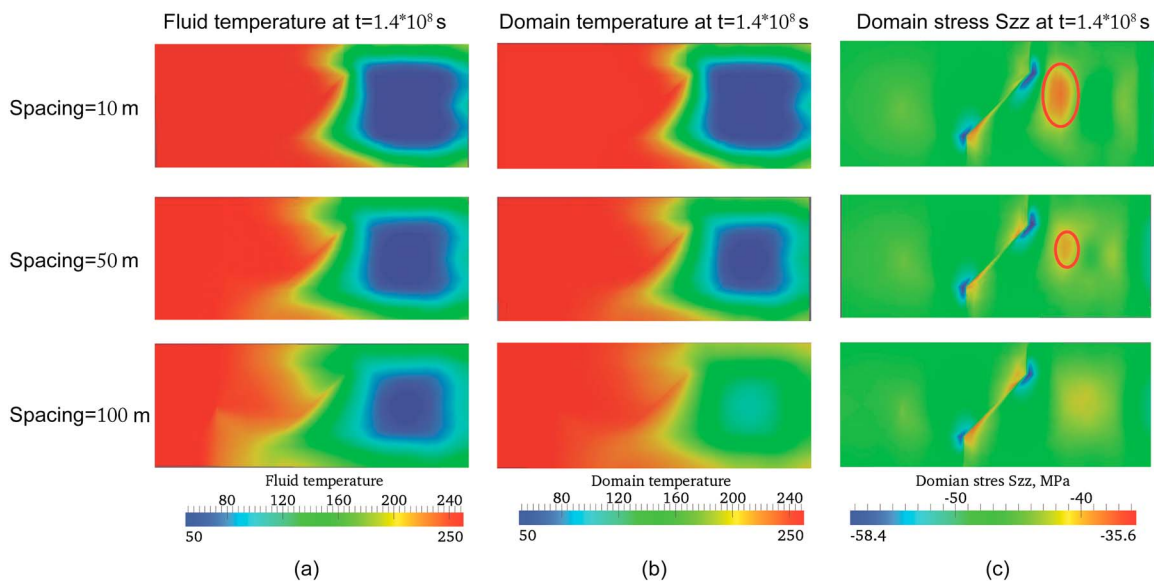

Figure 15. (a) Fluid temperature distribution at 4.4 years and 31 years under different fracture spacing (10 m-50 m-100 m) under the same injection pressure, (b) domain temperature comparison at 4.4 years under different fracture spacing (10 m-50 m-100 m), and (c) domain stress Szz at 4.4 years under different fracture spacing.
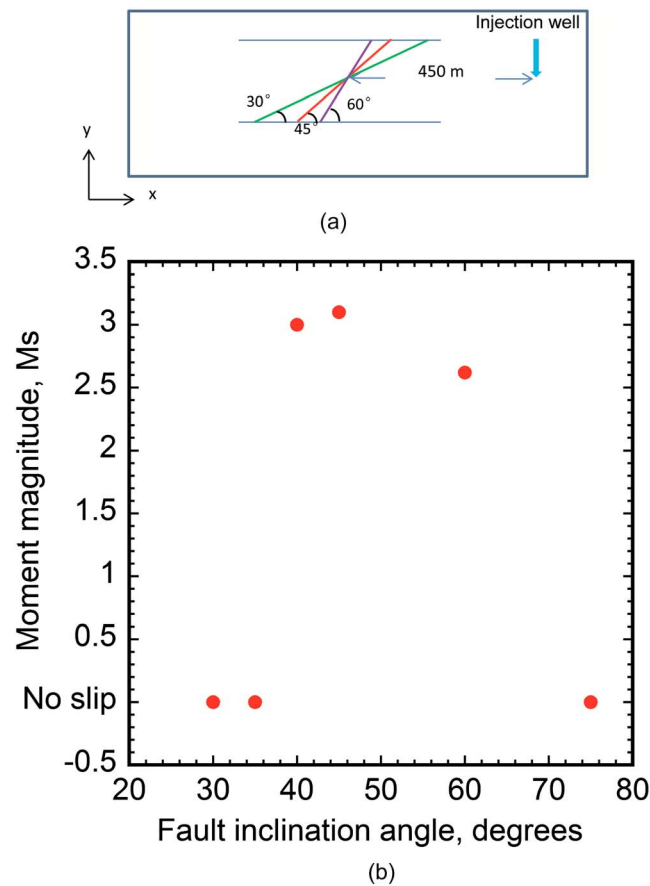
Figure 16. (a) Schematic figure of different fault inclination angles. (b) Fault seismic slip moment magnitude comparison under different fault inclination angles.

together with the critical controlling factors influencing slip magnitude and timing. The results indicate the primary influence of mechanical and hydrological effects in the short-term fault reactivation and the impact of thermal stress in causing long-term seismic slip.

The timing and magnitude of the initial H-M slip is insensitive to the permeability of the fault. This is because the transmission of fluid to the fault, from the injection well, is controlled by the permeability of the stimulated host medium. When the host fracture permeability is constant, the progression of the stress ratio between injection and fault due to hydraulic effect is similar in the magnitude and timing. Increasing the permeability of the host by an order of magnitude decreases the time to the first H-M event by an order of magnitude. For equivalent permeabilities, the rate of thermal recovery is controlled by the fracture spacing. Smaller fracture spacing results in faster thermal drawdown and more rapid energy recovery.

However, in terms of cold water injection, the induced thermal shrinkage stress does play an important role in unloading of the stress field by reducing the maximum in situ stress and thereby reduce the shear strength. This stress change is shown to result in secondary seismic slip, even when no strengthening of the fault is considered. The magnitude of the second seismic slip event is governed by the temperature difference between the injected fluid temperature and the ambient domain temperature. This is because the magnitude of thermal shrinkage stress is also proportional to the temperature difference. The larger temperature difference leads to a larger late stress ratio rise. In our results, where cold fluid is injected at 50°C, this results in a late stage event of $M_s = 2.6$ with a seismic slip distance of 6 cm. The fracture spacing does not affect the timing and magnitude of seismic slip when the permeability of the fractured medium is retained constant. This is surprising as the effectiveness of energy recovery and therefore the rate of cooling is increased with a decrease in fracture spacing. However, this does not significantly affect the timing of these secondary thermal events (Figure 14). Finally, the orientation angle of the fault directly determines the stress

state applied by the injected fluid and controls the magnitude of the resulting event, but not its timing. Faults with the largest stress obliquity fail with the largest moment magnitude.

References

Aki, K. (1967), Scaling law of seismic spectrum, *J. Geophys. Res.*, *72*(4), 1217–1231, doi:10.1029/JZ072i004p01217.

Bažant, Z., H. Ohtsubo, and K. Aoh (1979), Stability and post-critical growth of a system of cooling or shrinkage cracks, *Int. J. Fract.*, *15*(5), 443–456.

Biot, M. (1941), General theory of three-dimensional consolidation, *J. Appl. Phys.*, *12*(2), 155–164.

Boley, B. A. (1960), *Theory of Thermal Stresses*, John Wiley, New York.

Byerlee, J. (1978), Friction of rocks, *Pure Appl. Geophys.*, *116*(4–5), 615–626.

Caine, J. S., J. P. Evans, and C. B. Forster (1996), Fault zone architecture and permeability structure, *Geology*, *18*, 1025–1028.

Cappa, F. (2010), Modeling of coupled deformation and permeability evolution during fault reactivation induced by deep underground injection of CO_2, edited.

Cappa, F., and J. Rutqvist (2012), Seismic rupture and ground accelerations induced by CO_2 injection in the shallow crust, *Geophys. J. Int.*, *190*(3), 1784–1789.

Cappa, F., J. Rutqvist, and K. Yamamoto (2009), Modeling crustal deformation and rupture processes related to upwelling of deep CO_2-rich fluids during the 1965–1967 Matsushiro earthquake swarm in Japan, *J. Geophys. Res.*, *114*, B10304, doi:10.1029/2009JB006398.

Faulkner, D. R., A. C. Lewis, and E. H. Rutter (2003), On the internal structure and mechanics of large strike-slip fault zones: Field observations of the Carboneras fault in southeastern Spain, *Tectonophysics*, *367*(3–4), 235–251.

Garagash, D. I., and L. N. Germanovich (2012), Nucleation and arrest of dynamic slip on a pressurized fault, *J. Geophys. Res.*, *117*, B10310, doi:10.1029/2012JB009209,.

Jaeger, J. C. (1979), *Fundamentals of Rock Mechanics*, 3rd ed., Capman 1 Hall, New York.

Kanamori, H., and K. Abe (1979), Reevaluation of the turn-of-the-century seismicity peak, *J. Geophys. Res.*, *84*(B11), 6131–6139, doi:10.1029/JB084iB11p06131.

Kim, Y.-S., D. C. P. Peacock, and D. J. Sanderson (2004), Fault damage zones, *J. Struct. Geol.*, *26*(3), 503–517.

Miller, S. A., C. Collettini, L. Chiaraluce, L. Cocco, M. Barchi, and M. Kaus (2004), Aftershocks driven by a high-pressure CO_2 source at depth, *Nature*, *427*, 724–727.

Purcaru, G., and H. Berckhemer (1982), Quantitative relations of seismic source parameters and a classification of earthquakes, *Tectonophysics*, *84*(1), 57–128.

Rutqvist, J., and C. Oldenburg (2007), Analysis of cause and mechanism for injection-induced seismicity at the Geysers Geothermal Field, California, *GRC Trans.*, *31*, 441–445.

Rutqvist, J., Y.-S. Wu, C.-F. Tsang, and G. Bodvarsson (2002), A modeling approach for analysis of coupled multiphase fluid flow, heat transfer, and deformation in fractured porous rock, *Int. J. Rock Mech. Min. Sci.*, *39*, 429–442.

Rutqvist, J., J. Birkholzer, F. Cappa, C. Oldenburg, and C.-F. Tsang (2008), Shear-slip analysis in multiphase fluid-flow reservoir engineering applications using TOUGH-FLAC, edited.

Rutqvist, J., A. P. Rinaldi, F. Cappa, and G. J. Moridis (2013), Modeling of fault reactivation and induced seismicity during hydraulic fracturing of shale-gas reservoirs, *J. Pet. Sci. Eng.*, *107*(0), 31–44.

Sandwell, D. T. (1986), Thermal stress and the spacings of transform faults, *J. Geophys. Res.*, *91*(B6), 6405–6417, doi:10.1029/JB091iB06p06405.

Scholz, C. H. (1990), *The Mechanics of Earthquakes and Faulting*, Cambridge Univ. Press, Cambridge, New York, Port Chester, Melbourne, Sydney.

Segall, P., and J. R. Rice (1995), Dilatancy, compaction, and slip instability of a fluid-infiltrated fault, *J. Geophys. Res.*, *100*(B11), 22,155–22,171, doi:10.1029/95JB02403.

Streit, J. E., and R. R. Hillis (2004), Estimating fault stability and sustainable fluid pressures for underground storage of CO_2 in porous rock, *Energy*, *29*(9–10), 1445–1456.

Taron, J., and D. Elsworth (2009), Thermal–hydrologic–mechanical–chemical processes in the evolution of engineered geothermal reservoirs, *Int. J. Rock Mech. Min. Sci.*, *46*(5), 855–864.

Taron, J., and D. Elsworth (2010), Coupled mechanical and chemical processes in engineered geothermal reservoirs with dynamic permeability, *Int. J. Rock Mech. Min. Sci.*, *47*(8), 1339–1348.

Vermilye, J. M., and C. H. Scholz (1998), The process zone: A microstructural view of fault growth, *J. Geophys. Res.*, *103*(B6), 12,223–12,237, doi:10.1029/98JB00957.

Xu, T., E. Sonnenthal, N. Spycher, K. Pruess, G. Brimhall, and J. Apps (2001), Modeling multiphase non-isothermal fluid flow and reactive geochemical transport in variably saturated fractured rocks: 2. Applications to supergene copper enrichment and hydrothermal flows, *Am. J. Sci.*, *301*(1), 34–59.

Xu, T., J. A. Apps, and K. Pruess (2003), Reactive geochemical transport simulation to study mineral trapping for CO_2 disposal in deep arenaceous formations, *J. Geophys. Res.*, *108*(B2), 2071, doi:10.1029/2002JB001979.

Xu, T., E. Sonnenthal, N. Spycher, and K. Pruess (2004), TOUGHREACT User's Guide: A simulation program for non-isothermal multiphase reactive geochemical transport in variable saturated geologic media, Earth Sciences Division, Lawrence Berkeley National Laboratory, Univ. of California, Berkeley, Calif.

Zoback, M. D., and H.-P. Harjes (1997), Injection-induced earthquakes and crustal stress at 9 km depth at the KTB deep drilling site, Germany, *J. Geophys. Res.*, *102*(B8), 18,477–18,491, doi:10.1029/96JB02814.